Distinct Local Electronic Structure and Magnetism for Mn in Amorphous Si and Ge

Li Zeng[1†], *Juexian Cao*[2], *Erik Helgren*[1], *Julie Karel*[1], *Elke Arenholz*[3], *Lu Ouyang*[4], *David J. Smith*[4], *Ruqian Wu*[2], *Frances Hellman*[1*]

1. *Department of Physics, University of California, Berkeley, California, 94720 USA*

2. *Department of Physics and Astronomy, University of California, Irvine, California, 92697 USA*

3. *Lawrence Berkeley National Laboratory, Advanced Light Source, Berkeley, California, 94720, USA*

4. *Department of Physics, Arizona State University, Tempe, Arizona, 85287 USA*

[†] Current address: NSF Nano-scale Science and Engineering Center (NSEC), 3112 Etcheverry Hall, University of California, Berkeley, California 94720, USA

[*]email: fhellman@berkeley.edu

Transition metals such as Mn generally have large local moments in covalent semiconductors due to their partially filled *d* shells. However, Mn magnetization in group-IV semiconductors is more complicated than often recognized. Here we report the observation of a striking difference between Mn moments in amorphous Si (*a*-Si) and Ge (*a*-Ge) over a wide range of Mn concentrations (0.005-0.20). While Mn moments in *a*-Ge are large (≥3 μ_B), they are entirely quenched in *a*-Si (<0.1 μ_B). Corresponding differences are also observed in *d*-shell electronic structure, sign of Hall effect and atomic density. Density-functional-theory calculations show distinct local structures, and point to Mn coordination number as the key factor. Despite the amorphous structure, Mn in *a*-Si is in a relatively well defined high coordination, interstitial type site with broadened *d*-bands associated with low moment and electron (n-type) carriers, while Mn in *a*-Ge is in a low coordination, substitutional type site with large local moment and holes (p-type) carriers.

At the advent of the contemporary semiconductor era, transition metals (TMs) were viewed as undesirable impurities in group-IV semiconductors. Ludwig and Woodbury developed a model which successfully explained the electronic structure of TM impurities in crystalline Si (*c*-Si).[1] It is well established that ~10^{16}/cm^3 TM impurities create enough deep level states to significantly trap charge carriers and hinder transport.[2] More recently, exploration of novel ways to manipulate electron spins has made TM dopants of interest for spintronic applications, where both charge and spin are manipulated and utilized for information processing.[3-5] Magnetic semiconductors based on group-IV materials, like Si or Ge, are especially interesting due to their predicted high critical temperature T_c and predominance as mainstream semiconductor materials for microelectronics.

While Mn-doped *c*-Si and *c*-Ge have been made by various techniques, it has proven challenging to achieve robust intrinsic ferromagnetism at ambient conditions in either. First-principles calculations

suggest a local Mn moment for both interstitial and substitutional doping sites, and a high T_c in *p*-type Si or Ge.[6-8] However, magnetic properties reported in the literature, such as T_c and saturation moment, are very diverse even for samples prepared using similar methods. High T_c (up to 400 K) were reported for Mn doped in *c*-Si[9] and *c*-Ge,[8,10,11] but these samples were inhomogeneous, containing clusters,[11] nanocrystallites,[12,13] nanocolumns[10] or chemical inhomogeneity.[14] It is therefore difficult to know or understand the intrinsic magnetic properties.

To overcome these homogeneity issues, we have worked instead with an *amorphous* Si (*a*-Si) or Ge (*a*-Ge) matrix. For group-IV semiconductors, the amorphous structure preserves local tetrahedral four-fold covalent bonding, described by the continuous random network model.[15-18] Even when doped up to 20-25 at.% with atoms such as Nb, Y or the large magnetic rare-earth ion Gd, *a*-Si and *a*-Ge remain chemically homogeneous and amorphous, as measured by high resolution transmission electron microscopy, EXAFS, EDX, and other chemical and structural analysis tools.[19-21] These systems behave as excellent analogues (electronic and optical properties) to crystalline Si:P or Si:B, and have been used to probe many physics and materials science problems, including the T=0 insulator-metal (*I-M*) transition. The magnetic moment of Gd allowed detailed studies of a magnetic field-tuned *I-M* transition; these materials show enormous negative magnetoresistance (*MR*) at low temperatures, an indication of strong moment-carrier interactions and spin polarized carriers.[22,23] Ferromagnetism is robust to disorder, and the Mn moment should depend only on local environment, which for group-IV semiconductors is similar in crystalline and amorphous structures. Thus, there is no fundamental reason that the semiconductor matrix must be crystalline to give a magnetic semiconductor with spin polarized carriers, although high mobility conductivity would be precluded.[24-26] The great advantages to amorphous magnetic semiconductors are low growth temperature and the metastability of a homogeneous phase, inhibiting insolubility and phase-separation issues inherent in crystalline systems.

Here, we report unexpected and radically different magnetic and electronic properties of Mn-doped *a*-Si and *a*-Ge (*a*-Mn_xSi_{1-x} and *a*-Mn_xGe_{1-x}). Samples were prepared by *e*-beam co-evaporation under ultra high-vacuum conditions; details regarding sample preparation and characterization are in the Method section. For *x* ranging from 0.005 to 0.20, all samples are found to be homogeneous and amorphous despite Mn doping well above the solid solubility limit. We observe striking dissimilarities in magnetic properties: while a large Mn moment is observed in *a*-Ge, it is totally quenched (non-magnetic) in *a*-Si, leading to fundamentally different magnetic ground states and magneto-transport properties. These two "similar" systems have opposite signs of carriers and *MR*, and very different X-ray absorption spectra and concentration dependence of the atomic density. In this Article, we report systematic experimental studies of the structural and physical properties, as well as first-principles calculations to understand these differences, which are found to be exquisitely sensitive to the local atomic environment around Mn dopants.

We start with comparison of transport properties. Like doped crystalline semiconductors, an *I-M* transition is seen as a function of doping concentration *x* in both *a*-Mn_xSi_{1-x} and *a*-Mn_xGe_{1-x}. The three dimensional *I-M* transition is a quantum phase transition characterized by the ground state *dc* conductivity σ_{dc} at T=0. $\sigma_{dc}(T)$ as $T\rightarrow 0$ vanishes for insulators in an exponential form, while for metals it remains non-zero as $T\rightarrow 0$.[27] Figure 1 shows $\sigma_{dc}(T)$ for *a*-Mn_xSi_{1-x} and *a*-Mn_xGe_{1-x}; the data for each show a clear, monotonic increase with *x*, confirming the efficacy of Mn as a dopant in both matrices. The positive $d\sigma/dT$ is a signature of a disordered electronic system near the *I-M* transition.[27] The critical concentration x_C for the *I-M* transition is ~ 0.14 in both *a*-Mn_xSi_{1-x} and *a*-Mn_xGe_{1-x}, similar to other amorphous metal-doped semiconductors.[20,28] (x_C is enhanced by orders of magnitude compared to crystalline counterparts such as *c*-Si:P, due in part to strong charge carrier localization in the amorphous structure, and in part to differences in the depth of the dopant energy levels[29]) For a

given x, a-Mn_xGe_{1-x} has higher $\sigma_{dc}(T)$ than a-Mn_xSi_{1-x}, presumably because of the smaller band gap of Ge. Hall measurements were performed on metallic samples of each. Due to large carrier concentrations (~ $10^{22}/cm^3$) and longitudinal *MR* (positive for a-Mn_xSi_{1-x}; negative for a-Mn_xGe_{1-x}), carrier information was found from the asymmetry in the transverse resistivity $\Delta\rho_{xy}(H) = \rho_{xy}(+H) - \rho_{xy}(-H)$. $\Delta\rho_{xy}(H)$ is linear for both; the sign of the slope indicates electron-like and hole-like charge carriers in a-Mn_xSi_{1-x} and a-Mn_xGe_{1-x}, respectively.

Figure 2 (a) shows *dc* magnetic susceptibility $\chi(T)$ measured in 100 Oe field for typical a-Mn_xSi_{1-x} and a-Mn_xGe_{1-x} samples with similar x. The differences are striking: a-Mn_xGe_{1-x} has much larger $\chi(T)$, with a distinct cusp at a temperature T_f (~9 K for x=0.15) in the zero-field-cooled (ZFC) data. Field-cooled (FC) $\chi(T)$ is split from ZFC data below T_f. This suggests a spin-glass ground state for a-Mn_xGe_{1-x}, similar to Gd-doped (J=S=7/2) a-Si and a-Ge, resulting from competing ferromagnetic (FM) and antiferromagnetic (AFM) interactions.[17,28] Above T_f, $\chi(T)$ is well fit by a Curie-Weiss Law with large effective moment near that for S=3/2~5/2. By contrast, a-Mn_xSi_{1-x} has very small $\chi(T)$, fit well with a simple Curie law with low effective moment, and shows no sign of spin-glass freezing (down to 1.9 K, the lowest measured T).

Figure 2 (b) shows the field-dependence of magnetization per Mn atom [$M(H)$] for all a-Mn_xSi_{1-x} and a-Mn_xGe_{1-x} samples at T = 2 K, assuming all Mn atoms are equally magnetically active (this assumption is not likely true for a-Mn_xSi_{1-x} as will be explained later). There are a number of remarkable features to note. First, $M(H)$ is well below the Brillouin Functions (BF) for either S = 5/2 or 1/2 for both a-Si and a-Ge matrices, but, like $\chi(T)$, is significantly smaller for a-Mn_xSi_{1-x}, particularly for higher x, and with completely different dependence on x. Second, for a-Mn_xSi_{1-x}, dM/dH approaches 0 at high H, which is a sign of saturation, despite being well below the expected BF. Third, for a-Mn_xGe_{1-x} the small moment and significant slope dM/dH at high field despite the

large $\chi(T)$ can only be interpreted as due to strong frustrated magnetic interactions, consistent with the spin-glass freezing seen in $\chi(T)$.[30] The collapse of *a*-Mn_xGe_{1-x} $M(H)$ data, independent of x, indicates a similarity of Mn moments and interactions, similar to what was seen in *a*-Gd_xSi_{1-x} and *a*-Tb_xSi_{1-x}.[31]

The difference between the two systems is best seen in the x-dependence of effective moment p_{eff}, shown in Fig. 2 (c). p_{eff} is obtained by fitting $\chi(T)$ to a Curie-Weiss (CW) form: $\chi(T) = \frac{A}{T-\theta} + b$ ($T>T_f$ for *a*-Mn_xGe_{1-x}), with CW fitting constant $A = N_{Mn} p_{eff}^2 \mu_B^2 / 3k_B$, b = diamagnetic background constant, and N_{Mn} = number density of Mn atoms [determined by Rutherford backscattering (RBS) and film area]. For *a*-Mn_xGe_{1-x}, p_{eff} is $\geq 3\ \mu_B$, increasing with x to ~6 μ_B. In contrast, p_{eff} of *a*-Mn_xSi_{1-x} monotonically *decreases* and is negligible (less than 0.1 μ_B) at higher x. This small p_{eff} is consistent with the low saturation moment seen in Fig. 2 (b). A consistent fit of *all* *a*-Mn_xSi_{1-x} magnetic data is obtained by assuming an S=5/2 paramagnetic state, with a tiny fraction (~10^{-3}) of Mn being magnetically active and the majority of Mn *d* moments quenched.[32] The (small) positive *MR* seen at 2 K in *a*-Mn_xSi_{1-x} is thus simply explained – there are no moments and hence no significant moment-carrier interactions to produce negative *MR*, so *MR* is similar to that seen in other non-magnetic doped semiconductors. The negative *MR* in *a*-Mn_xGe_{1-x} is due to the same moment-carrier interactions and *I-M* physics as *a*-Gd_xSi_{1-x}; it is small (relative to *a*-Gd_xSi_{1-x}) because of increased AFM Mn-Mn interactions, reflected in the very low $M(H)$ shown in Fig. 2 (b).

X-ray absorption spectroscopy (XAS) at the Mn $L_{2,3}$ edges provides direct information about the *d* shell electronic structure that determines magnetism. Figure 3 shows XAS data for *a*-Mn_xGe_{1-x} and *a*-Mn_xSi_{1-x}, as well as results from Mn metal and Mn oxides for reference. *a*-Mn_xSi_{1-x} shows two broad, smooth absorption peaks with no atomic multiplet features, suggesting that the quenched Mn moment

in *a*-Si is due to itinerant *d* states existing even in a very insulating sample ($x \sim 0.005$).[33] The results are quite different for *a*-Mn_xGe_{1-x}, which shows distinct multiplet line-shape for all x. The absorption intensity of these data scales with x, with all *a*-Mn_xGe_{1-x} curves collapsing to a single line-shape similar to XAS reported for substitutional Mn in *c*-Ge[34,35].

Figure 4 (a) and (b) show high-resolution cross-sectional transmission electron micrographs for two typical samples of *a*-$Mn_{0.15}Si_{0.85}$ and *a*-$Mn_{0.19}Ge_{0.81}$. EDX scans were also performed to look for chemical inhomogeneity. No crystallinity or inhomogeneity was seen for any *a*-Mn_xSi_{1-x} or *a*-Mn_xGe_{1-x} (x<0.20). A very few places (diameters <2 nm) displayed suggestions of poorly defined lattice fringes, but digital diffractograms confirmed typical amorphous structure. These micrographs show no second phase or nanocrystallite formation commonly observed in crystalline films.[10-14] *a*-Mn_xSi_{1-x} and *a*-Mn_xGe_{1-x} samples are homogeneous and uniform to the microscope resolution limit of 0.17 nm, and differences in magnetization do not arise from micro-structural inhomogeneity.

The total number density n (atoms/cm^3) was determined by measuring areal density (atoms/cm^2) by RBS and thickness by atomic force microscopy; results are shown in Figure 4 (c). High quality pure *a*-Si and *a*-Ge films have n very close to their crystalline forms (~ 98%) because they preserve short-range tetrahedral ordering and have low vacancy concentrations.[15,36] Figure 4 (c) shows that $n(x)$ for *a*-Mn_xSi_{1-x} and *a*-Mn_xGe_{1-x} have the expected density at low x, but very different x dependence as x increases. $n(x)$ for *a*-Mn_xSi_{1-x} monotonically increases, while $n(x)$ for *a*-Mn_xGe_{1-x} has almost no x-dependence. If Mn dopants occupy interstitial-like sites, with no change in lattice spacing, $n(x)$ should increase with x, whereas $n(x)$ should be independent of x for the substitutional-like case. The data suggest that Mn atoms in *a*-Si are in an interstitial-like environment, while Mn atoms in *a*-Ge are in a substitutional-like environment, consistent with what has been suggested for crystalline counterparts at very low x.

Mn at interstitial-like sites would have more Si neighbours and stronger *p-d* hybridization, causing the *d*-band to lose its localized nature, similar to what occurs in weak itinerant metallic FM Mn-silicides ($MnSi_{1.7}$), in which M is tiny.[37] On the other hand, substitutional Mn in Ge is predicted to have a local moment of ~3 μ_B, [6,8] as was measured for the low x a-$Mn_{0.01}Ge_{0.99}$, and to act as a double acceptor, consistent with our Hall effect data. It is not clear why M per Mn increases with x in a-Ge, but the collapse of XAS data shows that this is not due to changes in 3d shell occupation of Mn. It may be due to polarization of hole-like carriers.

Experimental results from various measurements (transport, magnetic and structural analysis) thus paint a consistent picture that explains the difference in magnetism between a-Mn_xSi_{1-x} and a-Mn_xGe_{1-x}, two deceptively similar systems. We conclude that Mn occupies interstitial-like sites in a-Mn_xSi_{1-x} but substitutional-like sites in a-Mn_xGe_{1-x}. Over the wide Mn doping range studied (x=0.005~0.2), the monotonic x-dependencies of $\sigma(T)$, $\chi(T)$, and XAS intensity, as well as the x-independent $M(H)$ and XAS lineshape, all show that Mn is uniformly incorporated in each matrix. The qualitative differences in magnetization, and associated differences in *MR*, originate from different local atomic environments of Mn in each matrix.

To better understand and test this proposed model, first-principles calculations were carried out. The ability to interrogate local parameters in the simulated structure provides a powerful tool to probe correlations between local moment and local structure. Structural and electronic properties including local moments were calculated for three Mn concentrations, x=0.016, 0.094 and 0.156 (corresponding to N_{Mn} = 1, 6, 10 in a 64-atom supercell) for a-Si and a-Ge using *ab initio* molecular dynamics and solving the Kohn-Sham equations with the generalized gradient approximation (GGA). The amorphous structures were obtained by creating a supercell containing N_{Mn} Mn atoms plus (64- N_{Mn}) Si or Ge atoms randomly substituted on zinc-blende crystal structure sites. This initial configuration

was first "melted" at ~1800 K, then quenched at a rate of 2.4×10^{14} K/s to 600 K, then annealed for 10 ps at 600 K in the constant temperature [$NV(T)$] ensemble and finally quenched and relaxed to 0 K. The final configurations were further relaxed with an atomic force criterion that requires the calculated maximum force amplitude to be smaller than 0.01 eV/Å. Similar procedures have been extensively applied in studies of amorphous silicon.[38-40] To obtain reliable statistics, twenty independent initial configurations were used for each concentration. More details regarding calculations can be found in the Method section. For each concentration, the average magnetic moment M was calculated from $M = \frac{1}{N_{Mn}} \sum_{n=1}^{N} m_n \exp(\frac{E_n}{k_B T}) / \sum_{n=1}^{N} \exp(\frac{E_n}{k_B T})$, where N=20 is the number of configurations, and E_n and m_n are the total energy and magnetic moment for each final configuration. We find that M increases with x for a-Mn_xGe_{1-x}, but decreases with x for a-Mn_xSi_{1-x} to a very small value (0.043 μ_B for x=0.156), reproducing well the experimental data shown in Fig. 2.

To identify the origin of the vanishing magnetization in a-Mn_xSi_{1-x}, whether it stems from decrease of the local moment or cancellation through AFM coupling, we calculate and show in Fig. 5 the magnetic moment distribution function $\rho(m) = \frac{1}{N \cdot N_{Mn}} \sum_{n=1}^{N} \sum_{j=1}^{N_{Mn}} g(m - m_n^j)$, where m_n^j is the magnetic moment of the j-th Mn atom in the n-th final configuration and $\tilde{o}$-functions are represented by normalized Gaussian functions $g(z)$. $\rho(m)$ for a-Mn_xSi_{1-x} is predominantly at m = 0 μ_B, indicating zero local moment for the majority of Mn atoms in a-Si. Thus, the dramatic quench of magnetization in a-Mn_xSi_{1-x} is because of vanishing local moment. By contrast, the most probable m in a-Mn_xGe_{1-x} are in the range of 1.5 to 3.0 μ_B. Varying the supercell size (still with 64 atoms) from 10.95-11.54 Å (corresponding to mass densities 2.27-1.94 g/cm^3 for a-Si), which causes changes of interatomic spacing, was found to have only a small influence on M or $\rho(m)$ (less than 0.1 μ_B). Replacing Si by

Ge without altering the structure also does not alter M or $\rho(m)$. It is therefore clear that the lack of moment in a-Mn_xSi_{1-x} is not due to differences in Mn-Si/Mn-Ge distances or bonding chemistry, but lies instead in the different atomic arrangements of the two structures, which we next discuss.

Figure 6 (a) shows pair correlation functions (PCFs) for Mn-Si and Mn-Ge for x=0.094. The first peak locations, corresponding to the most probable nearest bond length, are slightly different due to the difference in Si and Ge atomic size. However, the quite different first peak *heights* show that Mn in Si has a significantly larger coordination number N_c (more Si nearest neighbours) than Mn in Ge. We define the coordination number N_c in these amorphous samples using the first minimum in the PCF as a cut-off distance. The inset shows Si-Si and Ge-Ge PCFs for the same concentration; these agree with typical values for a-Si and a-Ge, showing that the matrices are largely unaffected by Mn doping. Fig. 6 (b) shows the statistics for all Mn atoms in the 20 final configurations, indicating that Mn atoms mostly have 5 or 6 nearest neighbours in a-Ge but 7 or 8 nearest neighbours in a-Si. Fig. 6 (c) shows the local moment as a function of N_c. There is a strong correlation between N_c and the magnitude of the moment, essentially independent of whether the matrix is Si or Ge: Mn becomes non-magnetic for $N_c \geq 7$.

Finally, Fig. 6 (d) plots the spin up and spin down locally Projected Density of States (PDOSs) for three Mn atoms in a-$Mn_{0.094}Ge_{0.906}$ with different N_c. There is a large imbalance in PDOSs for the two occupied spin channels when N_c=5 or 6, which leads to a net moment for the majority of Mn in a-Ge. The imbalance decreases with N_c, and approaches zero when N_c=8, which is a rare configuration for a-Mn_xGe_{1-x} but the predominant configuration for a-Mn_xSi_{1-x}. Different N_c is thus the key parameter that leads to dramatically different magnetization for a-Mn_xSi_{1-x} and a-Mn_xGe_{1-x}. We also found that the number of electrons in Mn atoms increases with N_c,[41] suggesting that Mn atoms with N_c=7-8 provide electrons but those with N_c=4-5 provide holes, in good accord with

behaviour of Mn dopants at interstitial and substitutional sites, respectively. Furthermore, we found that Mn prefers geometries with N_c=4-6 in *a*-Ge, almost regardless of concentration. In contrast, for *a*-Si with x=0.094 and 0.156 most Mn atoms have N_c=6-8, while.at very low x, where the Mn-induced lattice distortion is rather limited, smaller N_c is found. It is known that Mn prefers substitutional sites in crystalline Ge and interstitial sites in crystalline Si, because of the smaller size of Si.[42,43] It appears that this difference is still present in amorphous structures.

In summary, Mn doping in amorphous group-IV semiconductors exhibits two distinct behaviours. The differences are due to high and low coordination Mn sites in Si and Ge, which result in, respectively, a quenched moment due to formation of itinerant states or a large local moment, further enhanced by interactions between moments and carriers. Transport, Hall Effect, XAS, atomic density, magnetization, and *MR* data are all explained by this model. The nature of Mn *d* electron states are known to be influenced by local atomic environment; here we have shown that the complete quenching of the Mn moment in Si and its preservation in Ge is directly linked to coordination number N_c. This helps to explain the wide variation of magnetization reported in the literature for Mn-doped crystalline Si and Ge, where local structure can differ even with similar preparation methods. While interstitial and substitutional sites for Mn are an obvious description for crystalline Si and Ge, depending on their relative atomic sizes, it is notable that the amorphous structures preserves this distinction. Control of the local environment, and specifically the need to have Mn in low coordination sites, is thus critical to a robust Mn moment and to making magnetic semiconductors.

Acknowledgement

Synthesis and some measurements were supported by NSF DMR-0505524. Characterization and work at the Advanced Light Source were supported by DOE Office of Basic Energy Sciences under

Contract DE-AC02-05CH11231. Work at UCI was supported by DOE grant DE-FG02-05ER46237. Calculations were performed on parallel computers at NERSC. We acknowledge use of facilities in the John M. Cowley Center for High Resolution Electron Microscopy at Arizona State University.

References

1. Ludwig, G. W. & Woodbury, H. H. Electronic structure of transition metal ions in a tetrahedral lattice. *Phys. Rev. Lett.* **5**, 98-100 (1960).
2. Weber, E. R. Transition metals in silicon. *Appl. Phys. A* **30**, 1-22 (1983).
3. Wolf, S. A. et al. Spintronics: a spin-based electronics vision for the future. *Science* **294**, 1488-1495 (2001).
4. Munekata, H. et al. Diluted magnetic III-V semiconductors. *Phys. Rev. Lett.* **63**, 1849 LP - 1852 (1989).
5. Ohno, H. et al. (Ga,Mn)As: A new diluted magnetic semiconductor based on GaAs. *Appl. Phys. Lett.* **69**, 363-365 (1996).
6. Stroppa, A. P., S.; Continenza, A. & Freeman, A. J. Electronic structure and ferromagnetic of Mn-doped group-IV semiconductors. *Phys. Rev. B* **68**, 155203 (2003).
7. Zhao, Y.-J., Shishidou, T. & Freeman, A. J. Ruderman-Kittel-Kasuya-Yosida-like ferromagnetism in Mn_xGe_{1-x}. *Phys. Rev. Lett.* **90**, 047204 (2003).
8. Park, Y. D. et al. A group-IV ferromagnetic semiconductor: Mn_xGe_{1-x}. *Science* **295**, 651-654 (2002).
9. Bolduc, M. et al. Above room temperature ferromagnetism in Mn-ion implanted Si. *Phys. Rev. B* **71**, 33302-1-4 (2005).
10. Jamet, M. et al. High-Curie-temperature ferromagnetism in self-organized $Ge_{1-x}Mn_x$ nanocolumns. *Nature Mater.* **5**, 653-659 (2006).
11. Li, A. P. et al. Magnetism in Mn_xGe_{1-x} semiconductors mediated by impurity band carriers. *Phys. Rev. B* **72**, 195205-1-9 (2005).
12. Awo-Affouda, C. et al. Observation of crystallite formation in ferromagnetic Mn-implanted Si. *J. of Vac. Sci. & Technol. A* **24**, 1644-1647 (2006).
13. Zhou, S. et al. Structural and magnetic properties of Mn-implanted Si. *Phys. Rev. B* **75**, 085203 (2007).
14. Kang, J.-S. et al. Spatial chemical inhomogeneity and local electronic structure of Mn-doped Ge ferromagnetic semiconductors. *Phys. Rev. Lett.* **94**, 147202 (2005).
15. Tanaka, K., Maruyama, E., Shimada, T. & Okamoto, H. *Amorphous Silicon* (John Wiley & Sons, 1999).
16. Haskel, D. et al. XAFS study of local disorder in the a-Gd_xSi_{1-x} amorphous magnetic semiconductor. *Phys. Rev. B* **67**, 115207-1-7 (2003).
17. Zeng, L. H., E.; Hellman, F; Islam, Rafiqul & Smith, David J. Growth and microstructure dependence of electronic and magnetic properties in magnetically doped Gd-Si amorphous semiconductors. *Phys. Rev. B* **75**, 184404-1-6 (2007).
18. Dalba, G., Fornasini, P., Grazioli, M. & Rocca, F. Local disorder in crystalline and amorphous germanium. *Phys. Rev. B* **52**, 11034 LP - 11043 (1995).
19. Hertel, G., Bishop, D. J., Spencer, E. G., Rowell, J. M. & Dynes, R. C. Tunneling and transport measurements at the metal-insulator transition of amorphous Nb: Si. *Phys. Rev. Lett.* **50**, 743 LP - 746 (1983).
20. Hellman, F., Tran, M. Q., Gebala, A. E., Wilcox, E. M. & Dynes, R. C. Metal-insulator transition and giant negative magnetoresistance in amorphous magnetic rare earth silicon alloys. *Phys. Rev. Lett.* **77**, 4652-5 (1996).
21. Hellman, F., Queen, D. R., Potok, R. M. & Zink, B. L. Spin-glass freezing and RKKY interactions near the metal-insulator transition in amorphous Gd-Si alloys. *Phys. Rev. Lett.* **84**, 5411-14 (2000).

22. Teizer, W. H., F. & Dynes, R. C. Magnetic field induced insulator to metal transition in amorphous-Gd_xSi_{1-x}. *Solid State Commun.* **114**, 81-6 (2000).
23. Teizer, W., Hellman, F. & Dynes, R. C. Spin Polarized Tunneling at the Metal-Insulator Transition. *Int'l J. of Mod. Physics B* **0**, 1-3 (2003).
24. Dietl, T. Ferromagnetic semiconductors. *Semicond. Sci. and Technol.* **17**, 377-392 (2002).
25. Moorjani, K. & Coey, J. M. D. *Magnetic glasses* (eds. Wolsky, S. P. & Czanderna, A. W.) (Elsevier, 1984).
26. Zallen, R. M. *Physics of Amorphous Solids* (Wiley, New York, 1983, 1983).
27. Lee, P. A. R., T. V. Disordred electronic system. *Rev. Mod. Phys.* **57**, 287 (1985).
28. Helgren, E. Z., L.; Sinenian, N.; Cherry, J. J.; Hellman, F.; Islam, R. & Smith, D. J. Magnetic and transport properties of amorphous Gd_xGe_{1-x} alloys near the metal-insulator transition. *Phys. Rev. B* **76**, 184440 (2007).
29. Anderson, P. W. Localized magnetic states in metals. *Phys. Rev.* **124**, 41 (1961).
30. Mydosh, J. A. *Spin glasses: an experimental introduction* (Taylor & Francis, London, Washington DC, 1993).
31. Liu, M. & Hellman, F. Magnetic and transport properties of amorphous Tb-Si alloys near the metal-insulator transition. *Phys. Rev. B* **67**, 54401-1-6 (2003).
32. Zeng, L. H., E.; Rahimi, M.; Hellman, F.; Islam, R; Wilkens, B. J.; Culbertson, R. J. & Smith, David J. Quenched magnetic moment in Mn-doped amorphous Si films. *Phys. Rev. B* **77**, 073306 (2008).
33. Zeng, L. et al. X-ray absorption study of the electronic structure of Mn-doped amorphous Si. *Appl. Phys. Lett.* **92**, 142503 (2008).
34. Picozzi, S. et al. X-ray absorption spectroscopy in Mn_xGe_{1-x} diluted magnetic semiconductor: experiment and theory. *Appl. Phys. Lett.* **86**, 062501 (2005).
35. Picozzi, S., Continenza, A. & Freeman, A. J. First-principles characterization of ferromagnetic Mn_5Ge_3 for spintronic applications. *Phys. Rev. B* **70**, 235205 (2004).
36. Laaziri, K. et al. High resolution radial cistribution function of pure amorphous silicon. *Phys. Rev. Lett.* **82**, 3460 (1999).
37. Gottlieb, U., Sulpice, A., Lambert-Andron, B. & Laborde, O. Magnetic properties of single crystalline Mn_4Si_7. *J. Alloys Comp.* **361**, 13-18 (2003).
38. Stich, I., Car, R. & Parrinello, M. Amorphous-silicon studied by *ab initio* molecular-dynamics - preparation, structure, and properties. *Phys. Rev. B* **44**, 11092-11104 (1991).
39. Car, R. & Parrinello, M. Structural, dymanical, and electronic properties of amorphous silicon: an ab initio molecular-dynamics study. *Phys. Rev. Lett.* **60**, 204 LP - 207 (1988).
40. Cooper, N. C., Goringe, C. M. & McKenzie, D. R. Density functional theory modelling of amorphous silicon. *Comput. Mater. Sci.* **17**, 1-6 (2000).
41. In their muffin-tin spheres of 1.323 Å in radius, Mn atoms have 5.5-5.7 electrons with *Nc*=4-5, but have 5.9-6.2 electrons with *Nc*=7-8.
42. Ludlam, J. J., Tarashin, S. N., Elliott, S. R. & Drabold, D. A. Universal features of localized eigenstates in disordered systems. *J. Phys. Condens. Matter* **17**, L321 (2005).
43. Wu, H., Kratzer, P., Scheffler M. Density-functional theory study of half-metallic heterostructures: interstitial Mn in Si. *Phys. Rev. Lett.* **98**, 117202 (2007).
44. Dong, J. & Drabold, D. A. Atomistic structure of band-tail states in amorphous silicon. *Phys. Rev. Lett.* **80**, 1928 (1998).

Figure 1 | Temperature dependence of dc conductivity $\sigma(T)$ for *a*-Mn_xSi_{1-x} and *a*-Mn_xGe_{1-x} for various concentrations *x* across the *I-M* transition. As *x* increases for each, the magnitude of $\sigma(T)$ increases monotonically and an *I-M* quantum phase transition is seen in both sets of samples, with critical concentrations x_c ~0.14 found by fits to low *T* data. σ increases with *T*, a result of localization and Coulomb effects in disordered electronic systems.

Figure 2 | Magnetic properties of *a*-Mn_xSi_{1-x} and *a*-Mn_xGe_{1-x}. (a) zero-field-cooled and field-cooled magnetic susceptibility $\chi(T)$ data for typical samples. For *a*-Mn_xSi_{1-x}, $\chi(T)$ is negligible compared to $\chi(T)$ of *a*-Mn_xGe_{1-x}. Inset shows the same *a*-Mn_xSi_{1-x} data on expanded scale. The red dashed line is a Curie fit. **(b)** *M* vs. *H* data measured at *T* = 2 K normalized to the number of Mn atoms. The dashed lines are Brillouin Functions (BFs) for *J*=*S*=5/2 and 1/2 and *g*=2 (pure spin state). For *a*-Mn_xGe_{1-x} samples, all $M(H)$ data collapse, are suppressed well below either BF and show no sign of saturation to *H*=6 kOe. For *a*-Mn_xSi_{1-x}, $M(H)$ data behave like free moments but with very small saturation moments (values dependent on *x* and less than 0.3 u_B); **(c)** Concentration dependence of effective moment p_{eff} of *a*-Mn_xGe_{1-x} and *a*-Mn_xSi_{1-x}, calculated from $\chi(T)$ data (above T_f for *a*-Mn_xGe_{1-x}) assuming all Mn are magnetically active. p_{eff} of *a*-Mn_xSi_{1-x} vanishes, distinct from the large p_{eff} of *a*-$Mn_xGe_{1-x,}$ which shows an increase with *x*. For *a*-Mn_xSi_{1-x}, a better and consistent fit for $\chi(T)$ and $M(H, T)$ is obtained by assuming S=5/2 for a tiny fraction of non-interacting Mn (~10^{-3}). For *a*-Mn_xGe_{1-x}, the distinct local moments interact with strongly mixed AFM and FM interactions, suppressing $M(H,T)$ far below the BF.

Figure 3 | X-ray absorption (XA) spectroscopy of Mn *L* edges in different materials. $L_{3,2}$ edges measure the transition from occupied *p* states to unoccupied *d* states. **(a)** Mn *L* edges of *a*-Mn_xGe_{1-x} resembles the spectra of Mn oxides, which show atomic multiplet features associated with localized *d* electronic states. The dash-dotted line is a simulated spectrum for $3d^5$. On the other hand, Mn in *a*-Mn_xSi_{1-x} resembles Mn metal films with smooth and broad *L* edges without any multiplet feature, but is different from Mn metal films in peak positions and peak width; **(b)** *L* edges of *a*-Mn_xGe_{1-x} for different *x* show the same multiplet lineshape. When normalized by the post-edge jump intensity, all *a*-Mn_xGe_{1-x} XA spectra collapse to the same curve. A typical XA spectrum of *a*-Mn_xSi_{1-x} (with two broad peaks,) is also plotted here to show the difference in lineshape. Due to different capping layer and surface sensitivity, *a*-Mn_xSi_{1-x} does not scale well with post-edge jump intensity for small *x*.

Figure 4 | Structural analysis of *a*-Mn_xSi_{1-x} and *a*-Mn_xGe_{1-x}. (a)-(b) High resolution cross-sectional transmission electron micrographs for *a*-$Mn_{0.15}Si_{0.85}$ and *a*-$Mn_{0.19}Ge_{0.81}$ samples showing an amorphous structure with no indication of any second phase or clustering; **(c)** total atomic number density as a function of concentration *x*. Symbols are data from RBS and thickness measurements (red and blue for *a*-Mn_xSi_{1-x} and *a*-Mn_xGe_{1-x} respectively). The red and blue dotted (dashed) lines are number densities calculated for interstitial (substitutional) Mn in Si and Ge respectively. For *a*-Mn_xSi_{1-x} samples, there is a strong concentration dependence matching closely the expectation for interstitial Mn in Si (with a constant n_{Si}), while for *a*-Mn_xGe_{1-x}, there is no concentration dependence, suggesting substitutional Mn in Ge.

Figure 5 | DFT results for magnetic moment distribution $\rho(m)$. For *a*-Mn_xSi_{1-x}, $\rho(m)$ is centred at zero moment, thus the lack of magnetization is due to lack of local moments instead of any AFM coupling. For *a*-Mn_xGe_{1-x}, significant moment distribution is between 1.5~3.0 μ_B with almost no distribution at low moment. Data are not shown for the lowest concentration x=0.0156, due to poor statistics (only 20 data points from one Mn atom in each 20 configurations)

Figure 6 | Pair correlation functions (PCFs), locally Projected Density of States (PDOS) on Mn, and statistics of local parameters as a function of the num`ber of nearest neighbours for Mn concentration x=0.094. (a) Mn-Si (red) and Mn-Ge (blue) PCFs. Inset: Si-Si (red dashed line) and Ge-Ge (blue dashed line) PCFs; **(b)** Statistical counts of the 120 Mn atoms in all 20 configurations (red and blue bars for Si and Ge respectively) and the average Mn-Si (red squares) and Mn-Ge distances (blue circles) d as a function of the number of Si or Ge nearest neighbours N_c ; **(c)** local Mn moment M in each matrix vs. N_c ; **(d)** PDOS for majority and minority spins of three Mn atoms with different N_c in *a*-$Mn_{0.094}Ge_{0.906}$.

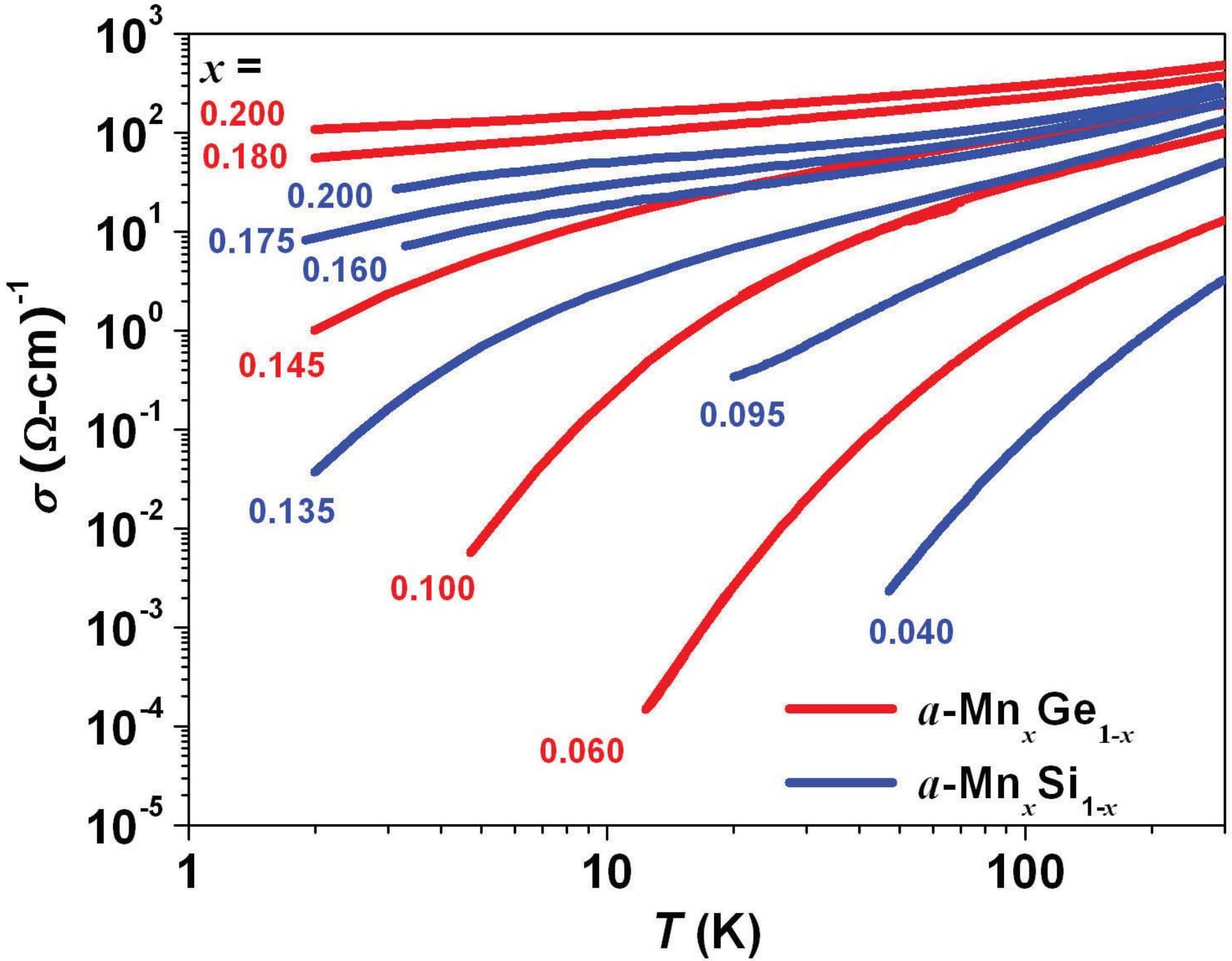
x =
0.200
0.180
0.200
0.175
0.160
0.145
0.095
0.135
0.100
0.040
0.060
a-Mn_x Ge_1-x
a-Mn_x Si_1-x
σ (Ω-cm)^-1
T (K)
10^3
10^2
10^1
10^0
10^-1
10^-2
10^-3
10^-4
10^-5
1
10
100

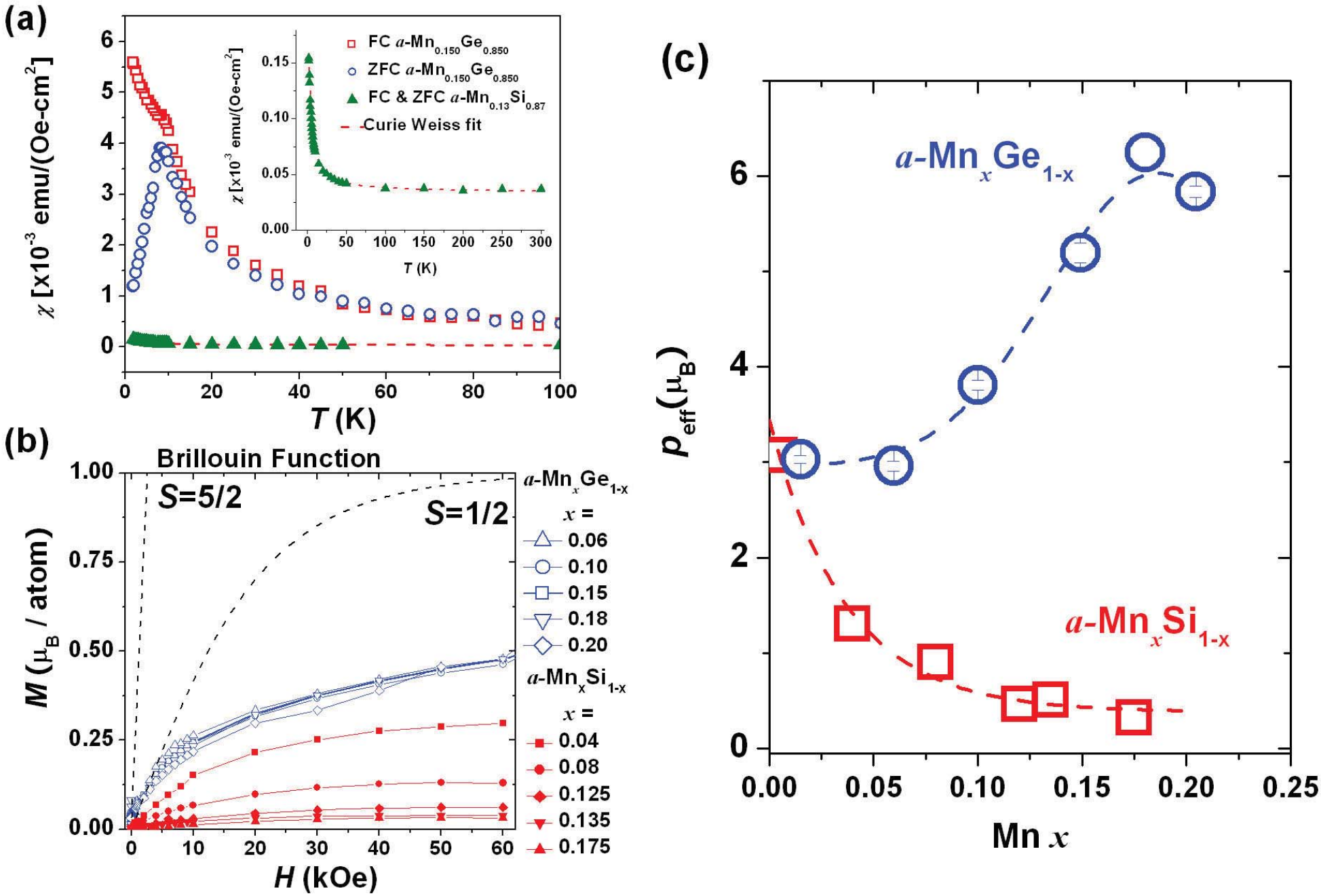
(a)
χ [x10^-3 emu/(Oe-cm^2)]
T (K)
FC a-Mn0.150Ge0.850
ZFC a-Mn0.150Ge0.850
FC & ZFC a-Mn0.13Si0.87
Curie Weiss fit
(b)
Brillouin Function
S=5/2
S=1/2
M (μB / atom)
H (kOe)
a-MnxGe1-x
x =
0.06
0.10
0.15
0.18
0.20
a-MnxSi1-x
x =
0.04
0.08
0.125
0.135
0.175
(c)
a-MnxGe1-x
a-MnxSi1-x
peff(μB)
Mn x

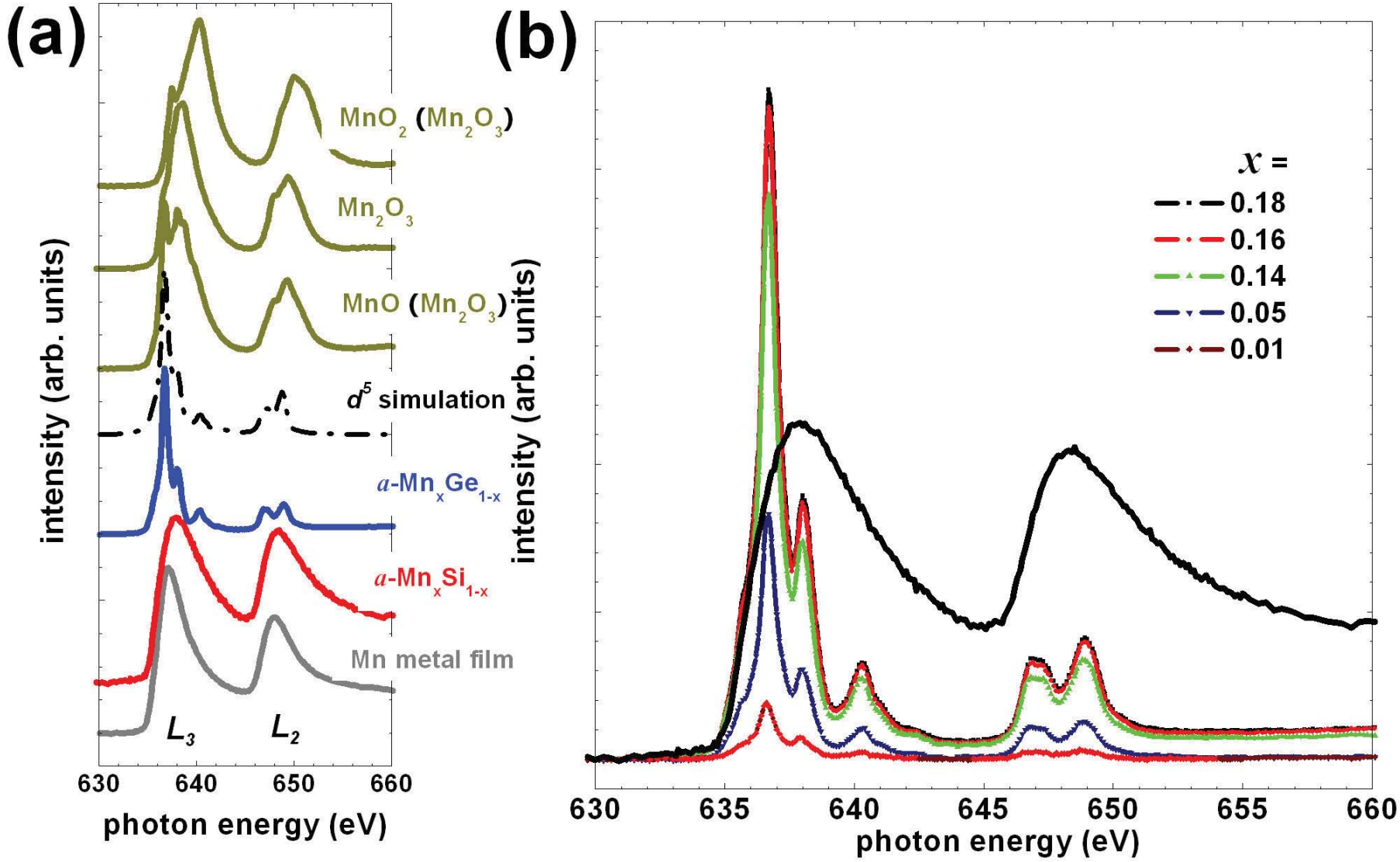
(a)
MnO2 (Mn2O3)
Mn2O3
MnO (Mn2O3)
d5 simulation
a-MnxGe1-x
a-MnxSi1-x
Mn metal film
L3
L2
intensity (arb. units)
630
640
650
660
photon energy (eV)
(b)
x =
0.18
0.16
0.14
0.05
0.01
intensity (arb. units)
630
635
640
645
650
655
660
photon energy (eV)

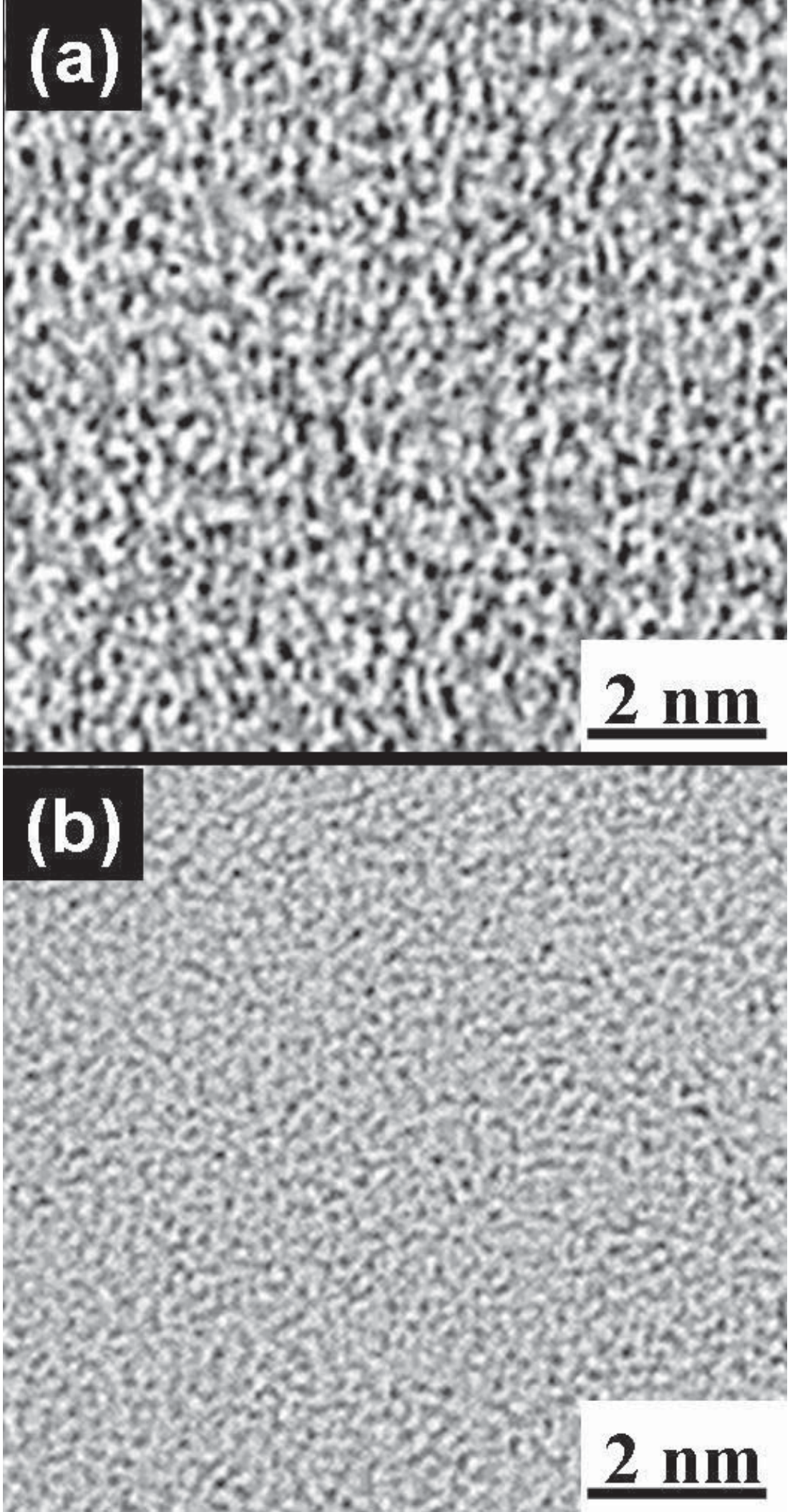
(a)
2 nm
(b)
2 nm

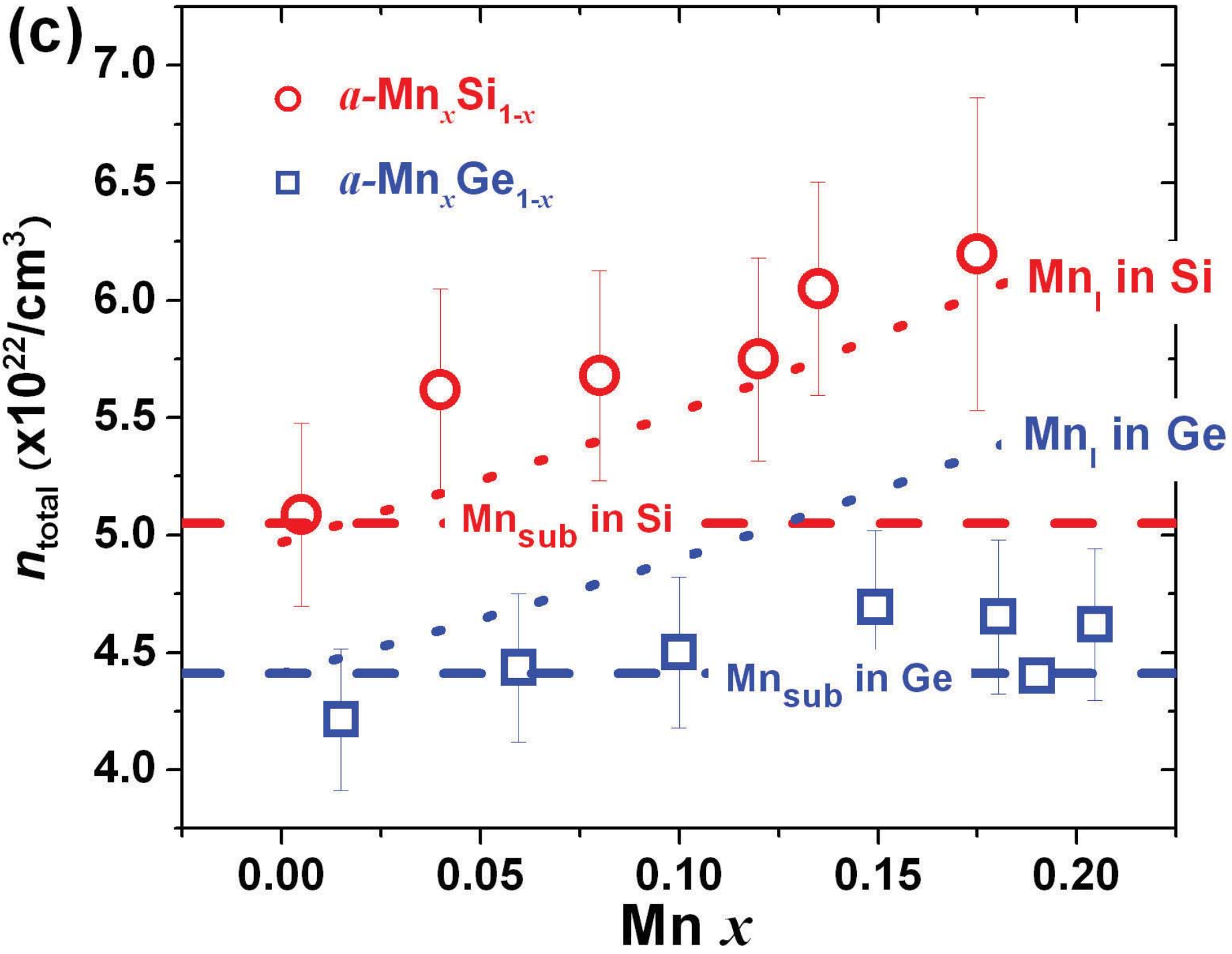
(c)
7.0
6.5
6.0
5.5
5.0
4.5
4.0
n_{total} (x10^{22}/cm^3)
a-Mn$_x$Si$_{1-x}$
a-Mn$_x$Ge$_{1-x}$
Mn$_I$ in Si
Mn$_I$ in Ge
Mn$_{sub}$ in Si
Mn$_{sub}$ in Ge
0.00
0.05
0.10
0.15
0.20
Mn x

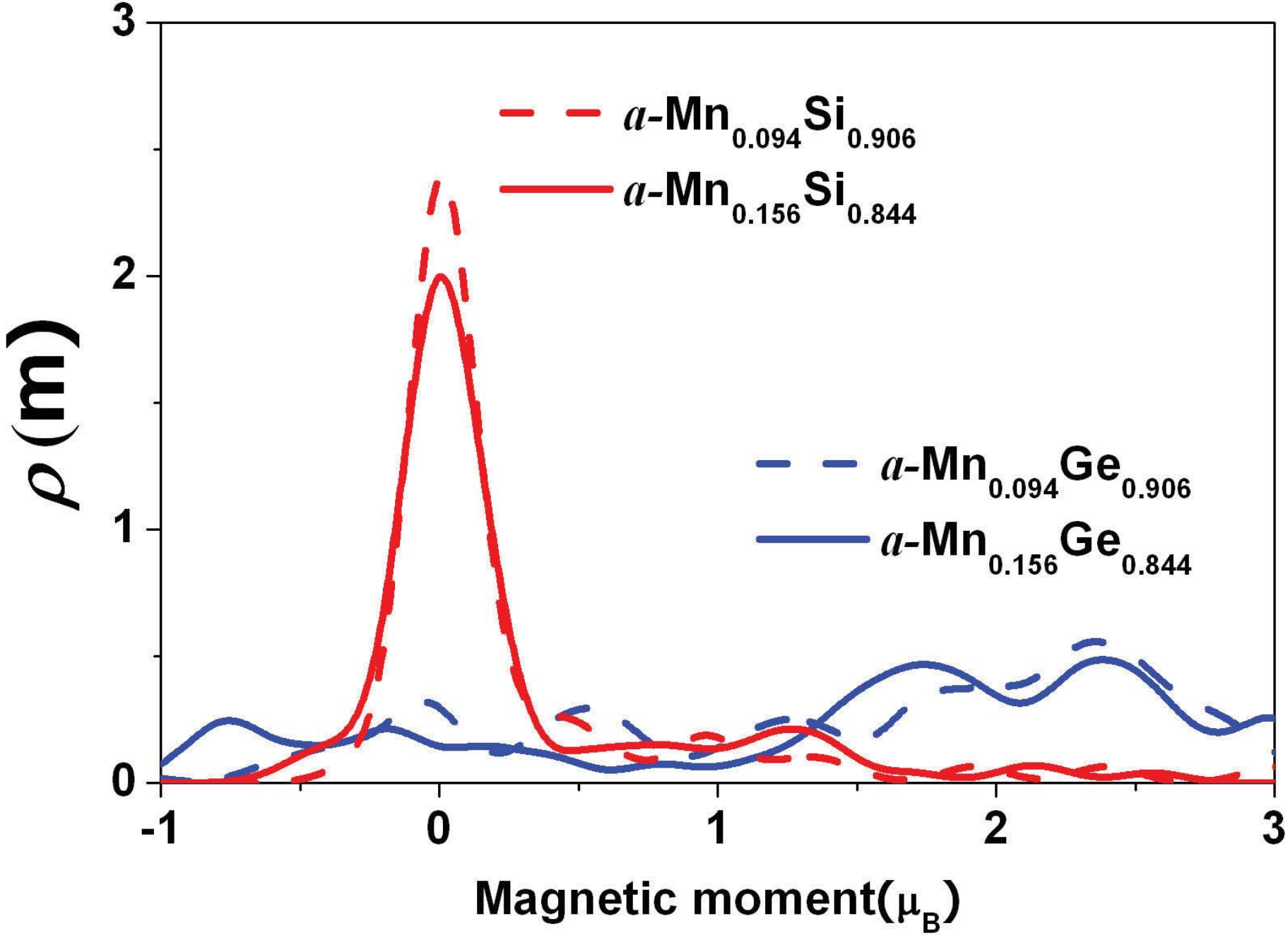
3
2
1
0
-1
0
1
2
3
ρ(m)
Magnetic moment(μB)
a-Mn0.094Si0.906
a-Mn0.156Si0.844
a-Mn0.094Ge0.906
a-Mn0.156Ge0.844

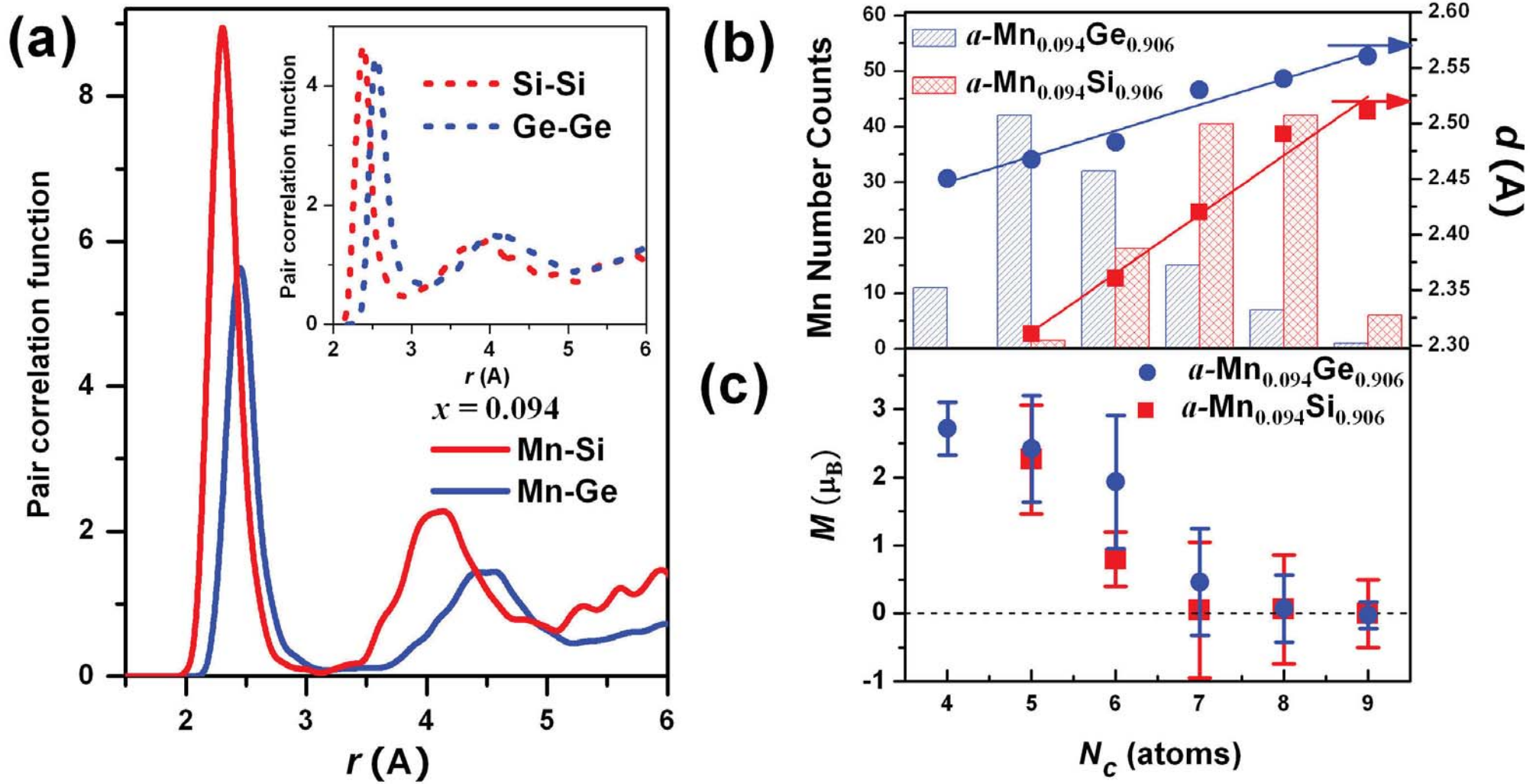
(a)
Pair correlation function
r (A)
Si-Si
Ge-Ge
Mn-Si
Mn-Ge
x = 0.094
(b)
Mn Number Counts
d (A)
a-Mn0.094Ge0.906
a-Mn0.094Si0.906
(c)
M (μB)
Nc (atoms)

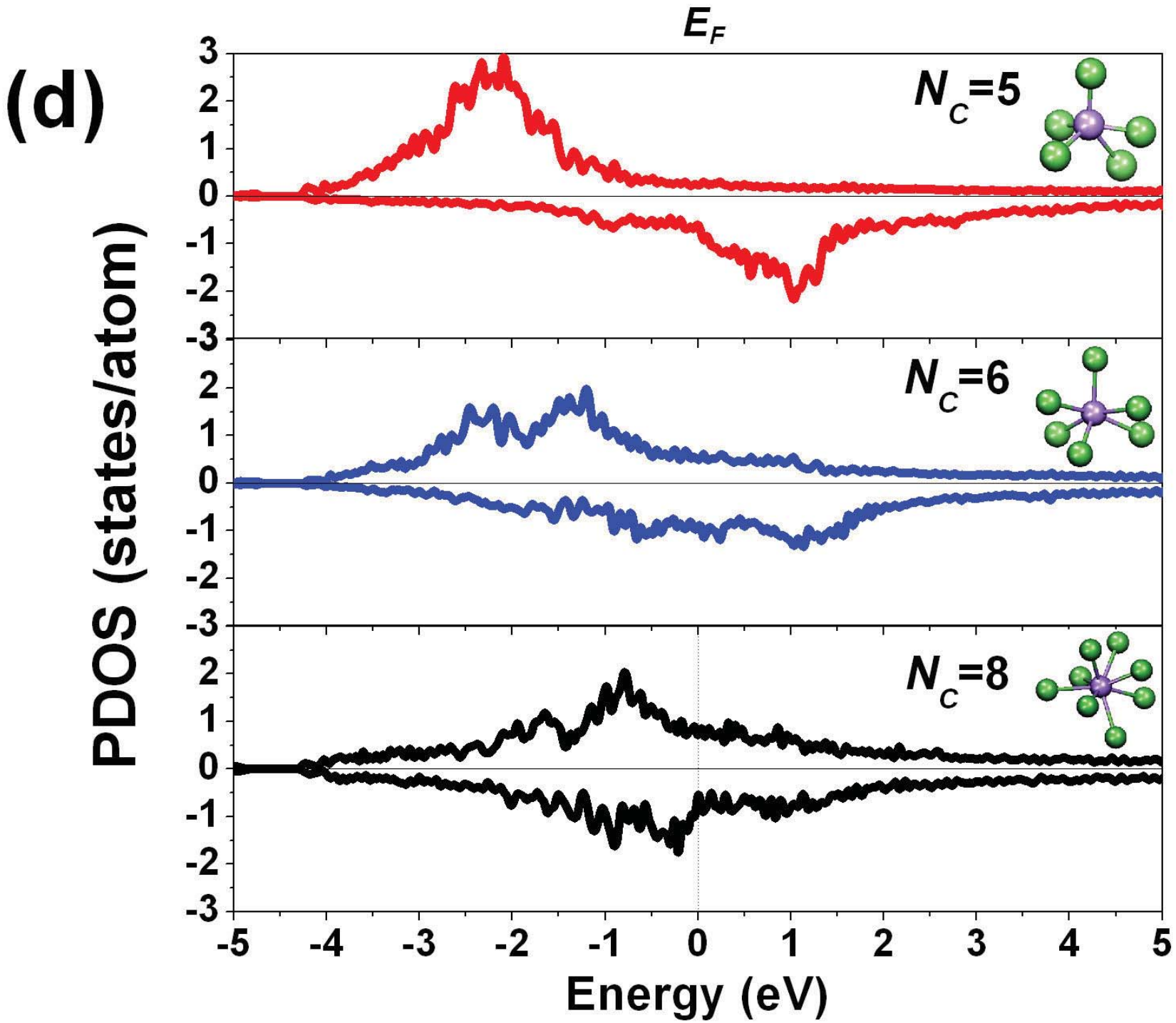
(d)
E_F
N_C=5
N_C=6
N_C=8
PDOS (states/atom)
Energy (eV)
3
2
1
0
-1
-2
-3
-5
-4
-3
-2
-1
0
1
2
3
4
5